Depth Analysis of Semi-Transparent Media by a Time-Correlated CMOS SPAD Line Sensor-Based Depth-Resolving Raman Spectrometer

Jere Kekkonen, Jan Nissinen, and Ilkka Nissinen, *Member, IEEE*

***Abstract*— Raman spectroscopy has proved to have potential in deep surface analytical applications. We present here, to the best of our knowledge, the first time depth analysis of semi-transparent media by a depth-resolving Raman spectrometer based on an adjustable time-correlated CMOS SPAD (single-photon avalanche diode) line sensor that can measure the depth of target samples embedded in a centimeter-scale semi-transparent medium simultaneously with a normal Raman depth profiling operation and suppress the fluorescence background by means of adjustable picosecond time gating. The variability of the depth derivation was measured to be ± 0.43 cm at depths ranging from 2 to 9 cm. In addition, the advantages of the adjustable picosecond time gating in terms of depth derivation and fluorescence background suppression performance were shown by comparing gate widths ranging from 100 ps to 13 ns. We believe that the technology concerned could pave the way for a new kind of compact, practical depth-resolving Raman spectrometer for deep subsurface analytical applications.**

***Index Terms*— Depth-resolving Raman spectrometer, depth analysis, time-correlated single photon counting (TCSPC), CMOS single-photon avalanche diode (SPAD).**

I. Introduction

RAMAN spectroscopy is a commonly used powerful non-invasive technique for resolving the molecular structure and chemical content of a material. Its potential for subsurface probing of turbid media in analytical applications has led to the development of various deep subsurface Raman spectroscopy techniques (DSRS), including confocal Raman microscopy, spatially offset Raman spectroscopy (SORS) and its daughter techniques (inverse SORS, surface enhanced SORS, μ-SORS and temperature SORS), transmission Raman spectroscopy, off-confocal Raman spectroscopy, cone-shell Raman spectroscopy, time-correlated Raman spectroscopy (TCRS), a combination of TCRS and SORS, frequency offset Raman spectroscopy (FORS) and hybrid FORS-SORS [1]–[14]. Most DSRS research to date has been concentrated on distinguishing the Raman spectra from different layers of diffusive bilayer samples with millimeter-scale layer thicknesses. The potential of DSRS has been demonstrated e.g. in medical diagnosis and disease monitoring, in the authentication of pharmaceutical products through packaging, the non-invasive detection of explosives, non-destructive food monitoring, the analysis of artworks and the analysis of multi-layered mineral samples [15]–[21].

The two most common DSRS techniques mentioned above are SORS (and its derivatives) and TCRS. A problem with SORS is that it requires multiple different spatial offset configurations to resolve the whole Raman depth profile of a sample [3]. Another problem with SORS, and with Raman spectroscopy in general, is the high fluorescence background of some samples, such as biological, mineral and explosive samples, that can partly or even totally mask the weaker Raman signal [22]–[24]. One method for overcoming the fluorescence problem is to use a pulsed laser and a time-gated detector, e.g. a gated intensified charged-coupled device (ICCD), or Kerr gate with a detector [25], [26]. Because the time responses of Raman scattering and fluorescence emission are different, the number of fluorescence photons can be effectively reduced if photons are collected only during a short time gate, as shown in Fig. 1(a).

Besides fluorescence suppression, these time-correlated techniques can also be used to probe and resolve the Raman depth profile of turbid and diffusive media [3], [11], [27]. The main aim of subsurface probing and Raman depth profiling is to distinguish the Raman spectra of different parts of a sample [3], [12], [28]. In time-correlated techniques, this Raman depth profiling is based on the temporal characteristics of photon migration in a medium, as depicted in Figs. 1(b) and 1(c) with two different time gate widths. Basically, the delay between the laser pulse and the times-of-arrival of the backscattered Raman photons (Rayleigh scattered photons are filtered by means of the dichroic filter and thus they are not shown in Fig. 1(b) to keep this principled figure as simple as possible) depends on the depth of the targeted part of the sample. An attempt is made to distinguish the Raman spectra of different parts of a sample (the top and bottom layers in Figs. 1(b) and 1(c)) by sweeping the time gate through the sample so that the delay between the trigger signal and the time gate opening is increased by means of delay unit until the Raman spectra of all the parts can be distinguished. In Fig. 1(c), for example, this means that during the time gate sweeping the Raman signal is mainly measured from the top layer of the bilayer sample when the first delay values are used (red pulse in Figs. 1(b) and 1(c)), and likewise it is mainly measured from the bottom layer of the bilayer sample (blue pulse in Figs. 1(b) and 1(c)) when the sweeping is continued and the second delay values are reached. As the

Manuscript received March 15, 2019; accepted April 18, 2019. Date of publication April 25, 2019; date of current version July 17, 2019. This work was supported by the Academy of Finland under Contract 314404 and Contract 292609. The associate editor coordinating the review of this paper and approving it for publication was Prof. Agostino Iadicicco. *(Corresponding author: Jere Kekkonen.)*

The authors are with the Circuits and Systems Research Unit, University of Oulu, 90014 Oulu, Finland (e-mail: jere.kekkonen@oulu.fi; jan.nissinen@oulu.fi; ilkka.nissinen@oulu.fi).

Digital Object Identifier 10.1109/JSEN.2019.2913222

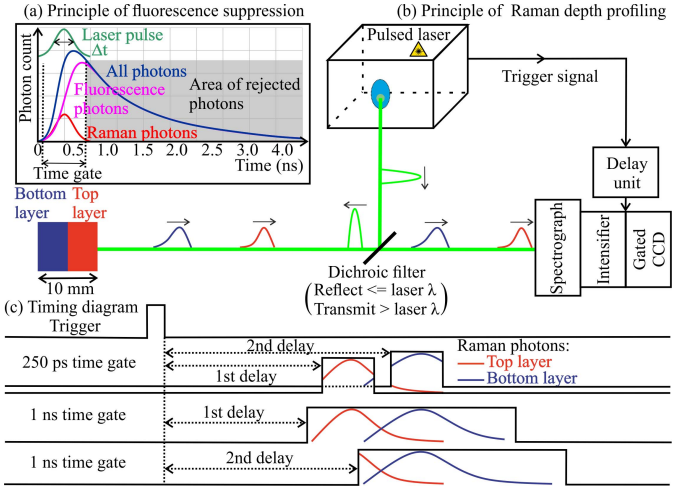

Fig. 1. (a) General principle of fluorescence suppression and (b) Raman depth profiling by means of a pulsed laser and time-gated ICCD and (c) a principled timing diagram with two time gate widths.

aim is simply to distinguish the Raman spectra of the different parts of the sample, the actual depths of the parts are not resolved in Raman depth profiling applications. To do this, precise information on the temporal distributions of the Raman photons would need to be measured, as will be shown later in this paper. In addition, the net (Raman) photon forward migration velocity inside the sample, which is affected by the random nature of the scattering in highly diffusive turbid samples, must be derived to resolve the depths of the different parts of a sample [12], [29]. The scattering and absorption caused by a turbid medium also affect the probability density function of the detected photons, because they modify both the ascending and descending edges of the probability density function and spread it as a function of depth, as illustrated with the Raman echo pulses in Figs. 1(b) and 1(c) [29], [30].

As can be seen from the time gate positions and Raman photon distributions in Fig. 1(c), the first gate position collects not only the Raman signal from the top layer but also some of the first Raman photons from the bottom layer, and likewise the second gate position collects not only the Raman signal from the bottom layer but also some of the late Raman photons from the top layer [12]. This effect is obviously much greater with longer time gate widths, as can be seen between the 250 ps and 1 ns time gates in Fig. 1(c), so that by the 1 ns time gate the whole Raman photon distributions of both layers fit inside the time gate. As mentioned above, the pure Raman spectra of the various parts of a sample need to be resolved to identify the different parts in Raman depth profiling. Therefore, a shorter time gate width can be said to enhance the depth profiling performance of a Raman spectrometer. Moreover, narrower instrument response functions (IRFs) can be obtained by means of a shorter time gate (with short laser pulses) and thus the depth of a Raman signal source can be derived more precisely, as shown in section III. B. of this paper. On the other hand, if a too short time gate is used, the total Raman photon distribution from the targeted part of the sample may not fit inside the time gate, as shown in the case of 250 ps gating in Fig. 1(c), leading to Raman signal loss, which may become a problem when measuring samples with low Raman signal levels.

Even though TCRS can yield more direct and precise depth information than SORS, the complexity of TCRS systems has hindered their widespread usage [30], [31]. Two recently suggested solutions for reducing the complexity of TCRS devices are a time-correlated single photon counting (TCSPC) silicon photomultiplier (SiPM) detector and a novel TCSPC camera, which works on the principle of a microchannel plate-based photomultiplier tube (MCP-PMT) [28], [32], [33]. The SiPM detector was a single-pixel detector that lacked simultaneous broadband spectrum acquisition and the system had some problems with the high noise of the detector, which might mask the weak Raman signal [32]. The limitations of the novel TCSPC camera were the need for additional acquisition electronics (because of the limited integration capability of MCP-PMT) and cooling to keep the thermal counts (noise) of the detector low enough [33].

To construct an even more compact, practical and cost-effective TCRS device, time-gated CMOS single-photon avalanche diodes (SPADs) could be used as the detector instead of the earlier mentioned techniques [34], [35]. The main advantages of CMOS SPAD-based detectors are that SPADs are able to detect digitally even single photons, synchronized measurements in which SPADs are biased to the Geiger mode (the mode in which SPADs can detect single photons) only during the laser pulse can be performed "more easily" compared to for example ICCDs, time gate resolution better than 100 ps can be achieved and the required TCSPC electronics can be integrated into the same die with a SPAD array (enabling broadband spectral acquisition) that will even further reduce the size and complexity of the whole device [34], [36]–[40]. Furthermore, we have already demonstrated the Raman radar functionality of a time-correlated CMOS SPAD-based Raman spectrometer with a distance resolution of 3.75 cm [41]. The same kind of time gate sweeping as described with the Raman depth profiling was used in that earlier study to gain the Raman radar functionality and thus, the earlier study gives some bases for this present study where Raman depth profiling by means of CMOS SPAD-based TCRS is studied. However, this paper presents more complex measurements compared to Raman radar operation. The Raman depth profiling requires a much better resolution of time gate sweeping than the Raman radar operation because the depth differences of samples were aimed to be measured with mm-level accuracy. In addition, there is only one object, which distance is derived based on the backscattered Raman photons traveling in the air, in radar operation, but in depth profiling, there can be multiple objects and different media, which optical properties affect to the trajectories of the photons, making the measurements much more complex. Furthermore, we are investigating here also how the different time gate widths are affecting the Raman depth profiling results with several samples, with and without fluorescence, embedded inside a medium.

We present here a depth-resolving Raman spectrometer based on a pulsed laser and an adjustable time-correlated CMOS SPAD line sensor with an off-chip delay unit that

allows sweeping of the time gate position with small delay steps (here 34 ps) and adjustment of the time gate width not only before the measurements but also in the data post-processing phase. The main aim is to demonstrate for the first time, to the best of our knowledge, the ability of such a device to assess the depths of target samples embedded in a centimeter-scale semi-transparent medium during a normal Raman depth profiling operation. In addition, different time gate widths and targets, with and without fluorescence, were used to show the advantages of the adjustable picosecond gating developed here in terms of depth derivation, Raman depth profiling (Raman spectra of different parts of a sample without any actual depth information) and fluorescence background (including the noise of the device) suppression performance. The concerned technique could open new possibilities for deep subsurface Raman spectroscopy in some application areas where transparent and semi-transparent media are analyzed, such as quality control in the food industry and nanocellulose manufacturing, and pave the way for the development of compact, practical depth-resolving Raman spectrometers that could measure the depths of target samples inside a centimeter-scale semi-transparent medium at the same time as performing a normal Raman depth profiling operation.

II. The Depth-Resolving Raman Spectrometer and Test Methods

A. A Time-Correlated CMOS SPAD Line Sensor-Based Depth-Resolving Raman Spectrometer

Block and timing diagrams of the developed depth-resolving Raman spectrometer based on an adjustable time-correlated SPAD line sensor are shown in Figs. 2(a) and 2(b), respectively. The spectrometer was originally designed to measure samples through a microscope objective, but in this work the objective was removed to be able to inject a collimated laser beam into a semi-transparent medium. The absence of the objective reduces the excitation and photon collection efficiency, but the main aim of this paper was to show the functionality of the mm-level depth-resolving Raman spectrometer based on time-correlated CMOS SPAD line sensor as a proof-of-concept. The excitation and photon collection efficiency without the objective could be improved by proper design of the optics.

The spectrometer consists of a 532 nm pulsed laser (Teem Photonics, model ANG500P-CHS), the necessary optics (a collimator, mirrors, beam splitters etc.), an optical detector, a laptop-controlled adjustable coaxial delay unit, a digital off-chip delay unit, a diffraction grating, a 16×256 CMOS SPAD-based line sensor with a 256-channel, 3-bit on-chip time-to-digital converter (TDC) and a computer and field-programmable gate array (FPGA) circuit. The pulse width, pulse energy, pulse rate and bandwidth of the laser were 160 ps (full width at half maximum, FWHM), 0.6 μJ, 350 kHz and 0.11 nm, respectively, and the pitch of the line sensor was 35.2 μm (active area of a single SPAD = 18 μm×18 μm), resulting in a wavenumber resolution of ~6 cm^{-1} (~0.2 nm). The FWHM of the IRF of the whole Raman spectrometer setup was measured to be 230 ps in [37] where is also a given detailed description of the 16×256 CMOS SPAD-based line sensor with a 256-channel, 3-bit TDC.

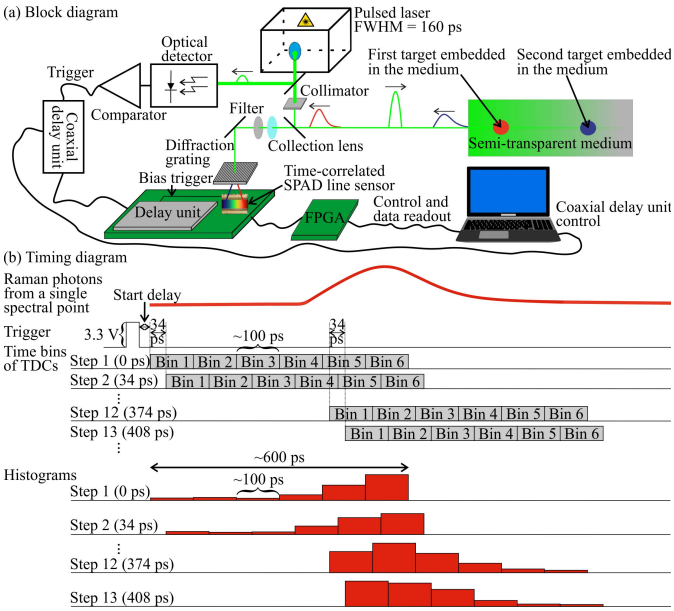

Fig. 2. (a) Block and (b) timing diagrams of the developed depth-resolving Raman spectrometer based on a time-correlated CMOS SPAD line sensor with example bin width and steps size of ~100 ps and 34 ps, respectively.

The sample is illuminated by collimated short laser pulses to derive a Raman spectrum. Raman scattered photons have different wavelengths and thus they diverge upon facing the diffraction grating so that the position of each SPAD in the line sensor corresponds to a specific range of wavelengths. The illumination of the sample and collection of the backscattered Raman photons happen through the same optical axis (reflectance configuration with zero source-to-detector distance). A small portion of the laser pulse is guided via a beam splitter to an optical detector coupled with a comparator that generates a logic level trigger signal passed through the delay units (coaxial delay unit and delay unit shown in Fig. 2(a)) with a low jitter to the CMOS SPAD line sensor. CMOS logic circuits integrated into the same die with the SPAD line sensor are used to bias the SPADs to the Geiger mode (CMOS logic circuits provide just the 3.3 V excess bias above the breakdown voltage of the SPADs). Neither the optical detector nor the delay units cause significant widening of the IRF of the whole Raman spectrometer setup because the IRF is dominated by the laser pulse width and the jitter of the SPADs (FWHM = 125 ps) resulting in $\sqrt{(160^2 + 125^2)} = 203$ ps, which is only 27 ps less than the FWHM of the total IRF of the system. This remaining width of the IRF is mainly explained by the jitter of the integrated TDCs.

To achieve depth scanning, the trigger signal can be delayed in arbitrarily defined steps by means of the adjustable air-insulated coaxial delay unit to collect only the photons arriving from the depth to be targeted, as shown in Fig. 2(b) where delay steps of 34 ps are used, for example. The length of the delay unit is adjusted by using a laptop-controlled stepper motor that rotates a thread rod enabling high-resolution low-jitter delay adjustment [42]. The dynamic range of the coaxial delay unit is only 850 ps and thus, to be able to use the whole dynamic range, an off-chip digital delay unit is used to compensate for the offset between the optical and electrical delays of the system and to roughly define the start location of

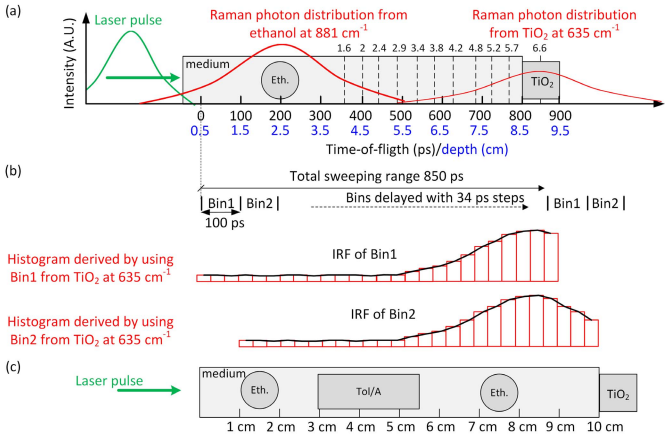

Fig. 3. (a) Sample configurations of the measurement where ethanol (Eth.) and TiO_2 targets were embedded in a semi-transparent medium and Raman photon distributions from ethanol and TiO_2 targets, (b) principle of IRF derivation by sweeping the bins of the TDCs (only bins 1 and 2 are shown here) and (c) sample configuration of the measurement where two ethanol, a mixture of toluene and acetonitrile (Tol/A) and TiO_2 targets were embedded in a semi-transparent medium.

the depth scans (start delay in Fig. 2(b)). Because the Raman spectrometer was originally designed to measure samples through a microscope objective, and thus the depth scanning functionality was not previously needed, the adjustable coaxial delay unit and the digital off-chip delay unit were added afterwards to achieve this scanning functionality.

Measurement of the time-of-arrival of the photons is started by means of the SPAD bias signal and ended by the photons of the echo pulse arriving in the bins of the TDCs located at each spectral point. The time domain histograms shown in Fig. 2(b) can be derived after several thousand laser pulses. The bins of the TDCs numbered from 1 to 6 are stabilized by a reference-locked delay line and their width can be adjusted to range from ~50 ps to ~200 ps. In addition, there is a longer bin 0, the width of which can be adjusted on a nanosecond scale due to the electrical structure of the time-correlated SPAD line sensor and bin 7 that is the over range bin used to detect the quenching signal generated by the CMOS logic to end the ongoing measurement cycle. Furthermore, the bins to be analyzed can be chosen in the post-processing phase, enabling different time-gate widths to be used in order to prove the advantages of the adjustable picosecond time gating in terms of depth derivation, Raman depth profiling and fluorescence background suppression performance as explained in more detail in section II C. A computer and an FPGA circuit control the programming of the detector electronics and read the measured time domain data from the detector chip. Post-processing of the measured data is performed by a Matlab (MathWorks) program to derive the basic raw Raman spectra and to smooth these spectra by removing the dark count noise and by filtering, for example.

B. Test Principles for Proving the Ability to Derive Depth Information on Targets Embedded in a Semi-Transparent Medium

1) Depth Scanning of Semi-Transparent Media: The semi-transparent media used in this work were colloidal firm jellies made up from water, gelatin and milk. The amount of water and gelatin in the media was constant but the amount of milk slightly varied between the media so that the milk-to-water ratio of the media varied from 4% to 5%. The absorption and reduced scattering coefficients of a medium with 5% milk-to-water ratio were estimated by using the time-domain diffuse optics method with the same laser as in the Raman measurements and a single-photon avalanche diode (Micro Photon Devices: PD100CTC) with a time-correlated single photon counting unit (Becker & Hickley GmbH: TCSPC Module SPC-130 EMN). The absorption and reduced scattering coefficients were estimated to be 0.01 mm^{-1} and 0.17 mm^{-1}, respectively. The derivation of the coefficients was based on the method presented in [43]. The refractive indices of the media with 5% and 4% milk-to-water ratio were estimated to be 1.40 and 1.31, respectively and the estimation procedure is presented below in section II. B. 2).

To prove that depth information on targets embedded in a semi-transparent medium can be derived by means of the time-correlated CMOS SPAD-based Raman spectrometer during normal Raman depth profiling, one target was embedded inside a jelly which the milk-to-water ratio was 5%, and another target was placed in contact with the rear edge of the jelly as shown in Fig. 3(a). The target inside the medium was pure ethanol in a cuvette (∅ ~1 cm) and the other target was titanium dioxide (TiO_2) powder in a cuvette (∅ ~1 cm). Reference Raman spectra for ethanol and TiO_2 can be found in [44] and [45], respectively. These targets do not have significant fluorescence emission and have the dynamic range of Raman intensity of 1:117. At the beginning of each depth scan, the start delay was adjusted by means of the digital delay unit so that the bins of the TDCs would collect photons from the medium before the ethanol target (it should be noted in Figs 3(a) and 3(b) that the time gate sweeping does not start at 0 cm but at 0.5 cm to be able to derive also the longest depth difference (6.6 cm) between the targets). After this, the bins were swept through the medium by increasing the delay in steps of ~34 ps by means of the coaxial delay unit and a Raman spectrum was measured at each step by shooting 2 million laser pulses at the sample, resulting in acquisition times of ~6 s with a pulse rate of 350 kHz. The total number of delay steps in each scan was 26, this being limited by the 850 ps dynamic range of the coaxial delay unit. After each scan a 0.4–0.6 cm (slice-to-slice variability) slice was cut from the rear edge of the medium. The TiO_2 target was then moved along the rear edge of the medium and the procedure was repeated. The total number of the depth scans was 11 and the sample configuration is depicted in Fig. 3(a) where the dashed lines indicate the depth difference between the targets at each depth scan. Photon counts for selected bins at a single spectral point were measured as a function of the delay steps to derive IRFs of the 881 cm^{-1} and 635 cm^{-1} Raman peaks of ethanol and TiO_2, respectively, as depicted in Figs. 3(a) and 3(b) with the 635 cm^{-1}Raman peak of TiO_2. The pulse energy of the laser was reduced to 0.3μJ in these measurements by means of a neutral density filter, because higher pulse energy, which can cause damage to some samples, was not needed here.

To further investigate the depth derivation capability of the time-correlated SPAD-based Raman spectrometer, four targets were embedded in a medium having a milk-to-water ratio of 4%. The targets (in order from the front edge of the medium) were ethanol, a mixture of toluene and acetonitrile (Tol/A), another ethanol target and TiO_2. The depths of the centres of the targets and the diameters of the targets were in the same order 1.5 cm, 4.25 cm, 7.5 cm and 10.5 cm and 1 cm, 2.5 cm, 1 cm and 1 cm, respectively. The sample configuration is also depicted in Fig. 3(c). The bins of the TDCs were swept through the medium and a Raman spectrum was measured at each step in the same way as for the measurement of two embedded samples described above, except that besides the IRFs of the Raman peaks of TiO_2 and ethanol, an IRF of 782 cm^{-1} Raman peak of Tol/A was also derived from the spectra. A reference Raman spectrum for Tol/A can be found in [46]. The bin width in both measurement set-ups described above was set to 100 ps and the measured data were analyzed using the photon count of a single bin (time gate width of 100 ps).

2) Derivation of Depth Information on Targets Embedded in a Semi-Transparent Medium: As our media were homemade, semi-transparent and the estimations for reduced scattering and absorption coefficients were quite low and thus they do not have a significant effect on the computation of depth information, we decided to derive the depth information on the targets simply based on the refractive indices of the media and targets and ignore the effects of low scattering of our media on the net photon migration velocity in the media. Statistics on photon penetration depths in random media and more sophisticated analytical forward solvers for Raman signals detected from homogenous diffusive media can be found in [29] and [30], respectively and these methods should be applied when media with higher scattering properties are measured.

The refractive indices of ethanol, toluene, acetonitrile and TiO_2 (rutile) for the laser wavelength used here (532 nm) are 1.36, 1.34, 1.50 and 2.54, respectively, and the mean of the refractive indices of acetonitrile and toluene, which is 1.42, was used as an estimate for the refractive index of Tol/A [47], [48]. The refractive indices of the semi-transparent media were estimated by measuring the IRFs of the 635 cm^{-1} Raman peak of TiO_2 through the media (target in contact with the rear edge) and from the same distance without the media. The speed of light in a medium was derived based on the length of the medium (round trip length) and on the differences between the delays in the peaks of the IRFs (difference in round-trip time-of-flight). The refractive index of a medium was derived from the speed of light in the medium by means of the equation $n = c/v$. The measured refractive indices of the media with 5% and 4% milk-to-water ratios were 1.40 and 1.31, respectively, and the sizes of the various components in the samples (the medium and the cuvettes) were considered when the average refractive indices of the whole samples were derived for a particular depth scan. The speed of light in a sample was derived based on this average refractive index of the sample and on the speed of light in a vacuum, after which the depths of targets were derived based on this estimated speed of light in the sample and on the delays in the peaks of the IRFs of the targets (round-trip time-of-flight). In addition, the depths of the centres of the targets were measured with a ruler as a "standard method".

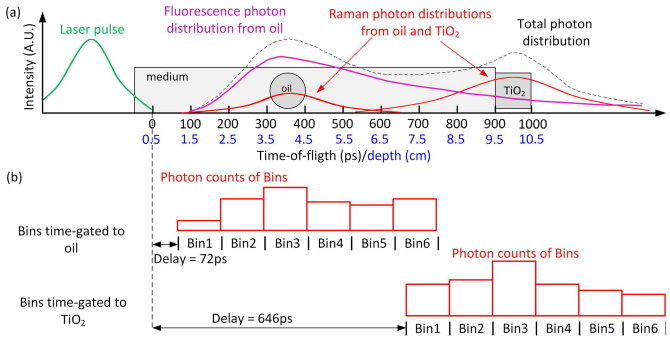

Fig. 4. (a) Sample configuration and photon distributions of the measurement where fluorescent samples (oil samples) and TiO_2 were embedded in a medium and (b) principle of time gating to the depths of the targets.

C. Test Principles for Evaluating the Effects of Time Gate Width on Depth Derivation, Raman Depth Profiling and Fluorescence Background Suppression Performance

Data from the depth scans of the medium in which the ethanol and TiO_2 targets were embedded and the medium was cut after every scan were analyzed not only by using the photon count of a single bin but also by taking the summed photon count of the bins 1-6, resulting in time gate width of ~600 ps in order to investigate the effects of time gate width on depth derivation and Raman depth profiling performance. As mentioned in the introduction, the main difference between these two terms is that in normal Raman depth profiling the absolute depths of the targets are not resolved but efforts are only made to distinguish the Raman spectra from different parts of the sample. To evaluate the fluorescence background suppression performance and to investigate further the effects of time gate width on Raman depth profiling performance, different time gate widths were used to measure the Raman spectra of the targets (Ø~1cm) with high fluorescence levels embedded alternately in a 9.5 cm long jelly medium with a milk-to-water ratio of 4% and a TiO_2 target was placed in contact with the rear edge of the medium as shown in Fig. 4(a). The targets with high fluorescence levels were olive oil and sesame seed oil, which have fluorescence-to-Raman photon ratios of 33 and 333 and fluorescence lifetimes of 2.5 ns and 2 ns, respectively [49]. Reference spectra for olive oil and sesame seed oil can be found in [37].

As can be seen from Fig. 4(a), the fluorescence decay of a fluorescent sample can mask the Raman signal of a deeper embedded target. The effect of fluorescence background on the Raman signals of the embedded targets can be suppressed by time gating the bins to the depths of the targets as shown in Fig.4(b). In addition, from Fig. 4(b) can be realized how the time gate width affect the fluorescence suppression, Raman signal-to-noise ratio (SNR) and Raman depth profiling performance. For example, if too wide time gate width is used (i.e. too wide and too many bins are summed to derive Raman spectrum), the sum of fluorescence photons can exceed the sum of Raman photons from a target and thus, totally mask the Raman signal. Too wide time gate width can also

collect Raman photons from both targets at the same time weakening the Raman depth profiling performance, but on the other hand, too narrow time gate does not collect the whole Raman signal from a target and thus the SNR decreases as was explained in the introduction. The time gate widths used in these measurements were 100 ps, 400 ps, 1.2 ns and 13 ns and these different time gate widths were achieved by modifying the widths of the bins of the TDCs and by selecting the bins to be analyzed in the data post-processing phase. The purpose of these configurations was to so show the advantages of the adjustable picosecond time gating achieved with the depth-resolving Raman spectrometer developed here relative to the longer constant-sized time gates used with time-gated ICCDs, for example.

III. Results and Discussion

A. Results of the Depth Derivation Measurements

The Raman spectra from selected depth scans of the medium in which the ethanol and TiO_2 targets were embedded and the medium was cut after every scan are shown in Figs. 5(a)–5(d). The depth difference between the targets in the selected depth scans were 5.2, 4.2, 3.4 and 2.4 cm, respectively. Since the intensity of the 144 cm^{-1} Raman peak of TiO_2 is much higher than that of any other, only the wavenumber range from 278 cm^{-1} to 1682 cm^{-1} is shown in the Figs., to make the spectra more readable. The spectra were obtained using only the photon count of bin 3 of the TDCs, resulting in a time gate width of ∼100 ps. As can be seen from the spectra, the intensity of the Raman spectrum of ethanol is the first to start increasing when the delay is increased, and after some point this intensity starts to decrease and that of the Raman spectrum of TiO_2 in turn starts to increase. When the delay has increased sufficiently, the intensity of the Raman spectrum of TiO_2 also starts to decrease, except in Fig. 5(a), where the limited range of the coaxial delay unit prevents the delay from increasing further. These findings are explained quite simply by the fact that the maximum intensity of the Raman signal is observed when the time gate position matches the depth of the target best, as this is where the Raman photons are generated by the peak amplitude of the laser pulse. This can also be clearly seen in the behavior of the spectra from the depth scan of the medium in which the Tol/A, TiO_2, and two ethanol targets were embedded, as shown in Fig. 5(e). These spectra were also obtained using only the photon count of bin 3. In addition, it can be seen from the spectra in Figs. 5(a)–5(d) that the intensity of the Raman spectrum of ethanol and the delay at which the maximum intensity of the spectrum is observed remain roughly the same between the depth scans but the intensity of the Raman spectrum of TiO_2 increases and the delay at which the maximum intensity of the spectrum is observed decreases when the medium is cut and the TiO_2 target brought closer, as could be predicted.

The IRFs of the 881 $cm^{-1}$and 635 cm^{-1} Raman peaks of ethanol and TiO_2 from the depth scans of the medium in which the ethanol and TiO_2 targets were embedded are shown in Fig. 6 to further emphasize the observations described above. The low variability seen in the IRFs of the ethanol target was expected, as the ethanol target was kept at a

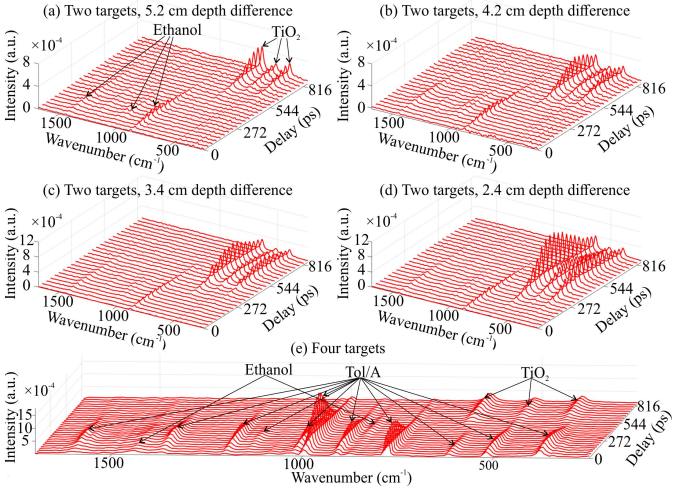

Fig. 5. (a)–(d) Spectra from selected depth scans of the medium in which the ethanol and TiO_2 targets were embedded, and (e) from the depth scan of the medium in which the Tol/A, TiO_2 and two ethanol targets were embedded. The spectra were obtained using the photon count of bin 3 of the TDCs (bin width ∼100 ps).

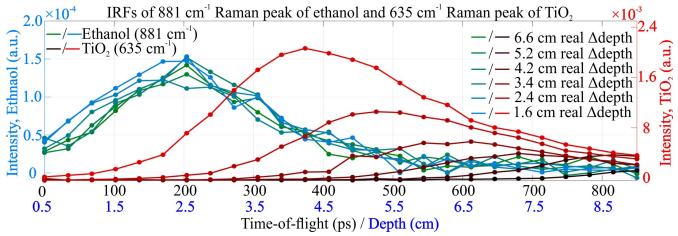

Fig. 6. (a) IRFs of the 881 cm^{-1} and 635 cm^{-1} Raman peaks of ethanol (green and blue lines) and TiO_2 (dark and red lines), respectively. The IRFs were obtained using the photon count of bin 3 of the TDCs (bin width ∼100 ps) and only the IRFs of every other depth scan are shown. Note that the depth scale is computed by using an average refractive index for all the depth scans and thus depth differences in this figure slightly vary from the actually derived depth differences that are computed by using weighted refractive indices for each depth scan as described in section II. B. 2).

constant depth, and likewise the high systemic variability seen in the IRFs of the TiO_2 target was expected, as the depth of the TiO_2 target was changed between the depth scans. These results show that it is possible to derive the depth of a target based on information on the delay in the peak of the IRF.

The IRFs of the 881 cm^{-1}, 635 cm^{-1} and 782 cm^{-1} Raman peaks of ethanol, TiO_2 and Tol/A, respectively, from the depth scan of the medium in which the Tol/A, TiO_2 and two ethanol targets were embedded are shown in Fig. 7. The IRFs in Fig. 7 were obtained by combining the photon counts of bins 2, 3, and 4 to enlarge the time range, which is limited to 850 ps when only one bin is used due to the limited dynamic range of the coaxial delay unit. The enlargement of the time range was achieved by covering the time range 0-102 ps by the photon count of bin 2, the time range 102-952 ps by the photon count of bin 3 and the time range 952-1054 ps by the photon count of bin 4. This idea can be understood by examining Figs. 3(a) and 3(b) where bin 1 could be used to cover the beginning (0-102 ps) of the time range, bin 2 could be used to cover the midrange (102-952 ps) and bin 3, which is not shown, could be used to cover the end (952-1054 ps)

of the time range. Note that bins 1 and 3 would also cover most of the midrange and thus, this overlapping could be used in the averaging of results as discussed more detailed below. Not only do these IRFs further confirm the concept of depth derivation explained above, but they also show that it is possible to derive the depths of targets made from the same substance (here ethanol) based on information on the delays in the local peaks of the IRF. As can be seen in Fig. 7, the local peak in the IRF caused by the first ethanol target has already decreased to around its minimum value before the second peak caused by the second ethanol target starts to increase, implying that the depth separation of the ethanol targets could have been much less than the 6 cm used here and the local peaks would have been still distinguished. One more observation regarding the IRFs shown in Fig. 6 and 7 concerns the widening of the IRFs (IRF of the spectrometer ~230 ps), which indicate the presence of absorption and scattering in the samples even if the reduced scattering and absorption coefficient of the samples were estimated to be quite low.

The depth information in this work was derived between two targets and not from the front edge of the medium, as this is a proof-of-concept paper and it is easier and more convenient to derive the depths of targets based on delays in the peaks of IRFs than to determine the location of the front edge of a medium. The media used do not have (observable) Raman peaks as can be noticed from Fig. 5, and thus the IRFs caused by the media cannot be derived in the same way as with the targets. The background level of the media, which is mainly caused by the faint fluorescence of the media that is not even observable in Fig. 5, is higher than that of pure air. Therefore, the IRF caused by a medium could be possibly derived based on this difference in background level, and thus the location of the front edge of the medium could be derived from the rising edge of this IRF.

The depth differences between the ethanol and TiO_2 targets in the measurements where these two targets were embedded in the medium and the medium was cut after each depth scan were derived from the delay differences between the peak values of the IRFs of the targets (TiO_2 - ethanol), as explained in section II. B. 2). The variability of the depth derivation was measured to be $\pm$ 0.43 cm in these depth scans. The left-right arrows in Fig. 7 show to derived and real depth differences between the targets in the depth scan of the medium in which the four targets were embedded. The variability of the depth derivation was measured to be $\pm$ 0.41 cm in this depth scan when the IRFs were obtained by using the combined photon counts of bins 2, 3 and 4 as explained above. If the depth differences between targets are first derived only by using single bins 2, 3 and 4 and then averaged, the variability of the depth derivation is only $\pm$ 0.18 cm in this depth scan. The averaging is possible due to overlapping of the time ranges of the bins in the time gate sweeping as explained above.

The most obvious reason for variability in the derived depth information is the finite size of the delay steps that defines the resolution of the depth scans. Smaller steps could have led to a better resolution and thus more accurate results. Other possible means of improving the precision and accuracy of

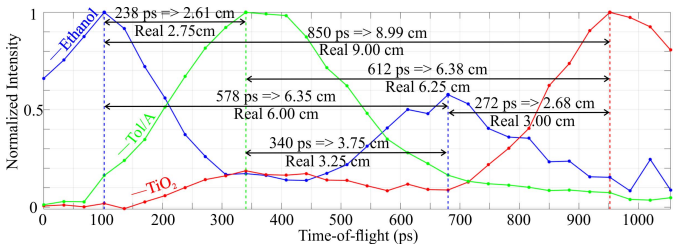

Fig. 7. IRFs of the 881 cm^{-1}, 635 cm^{-1} and 782 cm^{-1} Raman peaks of ethanol, TiO_2 and Tol/A, respectively, from the depth scan of the medium in which the Tol/A, TiO_2 and two ethanol targets were embedded. The left-right arrows show the derived and real depth differences between the targets. The IRFs were obtained by combining the photon counts of bins 3, 2 and 4 of the TDCs (bin widths ~100 ps) to enlarge the time range as explained in the text.

the determination of the peaks of the IRFs would have been to fit, for example, a Gaussian model based on the measurement points to describe the IRFs and/or to use narrower laser pulses and a shorter time gate. Another possible reason for variability in the derived depth information could have been error in the estimation of the refractive indices of the media and of the whole samples. Estimation of the refractive indices of the samples also imposes a limitation on the method used to derive the depths of targets from the application point of view, as it requires additional information on the dimensions of the different components of the sample. It is therefore evident that more adequate techniques are needed for estimating the refractive indices. One possibility would be to employ the methods that could derive the depth information based on the measured estimations of the absorption and reduced scattering coefficients [29], [30]. This would have been necessary if samples with higher scattering properties, such as biological tissues, would have been measured.

B. Effects of Time Gate Width on Depth Derivation, Raman Depth Profiling and Fluorescence Background Suppression Performance

The IRFs of the 881 cm^{-1} and 635 cm^{-1} Raman peaks of ethanol and TiO_2 obtained from the depth scan of the medium in which the ethanol and TiO_2 targets were embedded and the medium was cut after every scan are shown in Fig. 8. These IRFs were obtained by summing the photon counts of bins 1-6 resulting in time gate width of 600 ps. Comparing Fig. 8 with Fig. 6 it becomes noticeable how the IRFs spread as the time gate width is increased. The explanation for this observation is that a shorter time gate follows the shape of the Raman echo pulse better than a longer time gate does. Thus, the peaks of the IRFs flatten out with a longer time gate because a longer time gate collects the same quantity of Raman photons from the target over a longer time during the time gate sweeping than a shorter time gate does. The flattening of the peaks is obviously problematic when deriving depth information, because we cannot conveniently derive the locations of the peaks in the IRFs, as can be observed in Fig. 8.

The longer time gate width also leads to a situation in which the delay range from which photons are gathered from both targets at different depths is longer. In other words, this means that the delay range in which the intensity of the IRFs of both

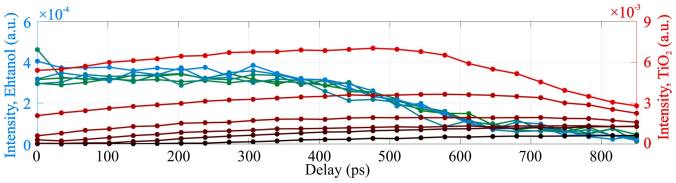

Fig. 8. IRFs of 881 cm^{-1} and 635 cm^{-1} Raman peaks of ethanol (green and blue lines) and TiO_2 (dark and red lines) from the depth scan of the medium in which the ethanol and TiO_2 targets were embedded. IRFs were obtained by using the summed photon count of bins 1-6 resulting in time gate width of 600 ps. The color codes of the IRFs are the same as in Fig. 6 and only the IRFs of every other dept scan are shown.

the ethanol and TiO_2 targets is high is longer with a longer time gate, as can be seen in Fig. 8. Overlapping of the IRFs is problematic in Raman depth profiling of samples as it means that the signal is gathered from both targets and pure spectra, which are desired in Raman depth profiling, are unachievable. This effect can be seen also in Figs. 9(c) and 9(d), where the Raman spectra of the TiO_2 and olive oil targets embedded in the semi-transparent medium at depths of 3.5 cm and 9.5 cm, respectively, were obtained using a time gate width of 400 ps first time-gated to the olive oil target (Fig. 9(c)) and then to the TiO_2 target (Fig. 9(d)). Even if the time gating was applied to a specific target, some features of the spectra of both targets can be seen in both measured spectra.

Figures 9(a)–9(l) shows the spectra from the measurements in which alternately olive oil (Figs. 9 (a)–9(f)) and sesame seed oil targets (Figs. 9(g)–9(l), a decade higher fluorescence-to-Raman ratio compared to olive oil) were embedded in the medium alongside the TiO_2 target and the spectra were obtained using time gate widths of 100 ps (Figs. 9(a), 9(b), 9(g), 9(h)), 400 ps (Figs. 9(c), 9(d), 9(i), 9(j)), 1.2 ns (Figs. 9(e), 9(k)) and 13 ns (Figs. 9(f), 9(l)) to investigate the effects of time gate width not only on Raman depth profiling performance but also on the fluorescence background suppression performance. From all the spectra shown in Fig. 9 can be noticed the overlapping of the fluorescence decay of the oil targets with the Raman scattering from the deeper TiO_2 target (see Fig. 4(a) in section II. C.) that causes the seen increase of the overall intensity level, which steepens towards higher wavenumbers because of the fluorescence emission profiles of oil targets.

Distinguishable spectra of TiO_2 were achieved with the time gate widths of 100 ps and 400 ps time-gated to TiO_2 with both fluorescence background levels as can be seen in Figs. 9(b), 9(h), 9(d) and 9(j), but as mentioned above, the purity of the spectra is lost with the gate width of 400 ps. In addition, the two highest Raman peaks of olive oil can be distinguished using the time gate widths of 100 ps and 400 ps time-gated to olive oil as shown in Figs. 9(a) and 9(c). The Raman spectrum of sesame seed oil cannot be distinguished with certainty with any of the time gate configurations, but some hints as to its Raman peak at 1442 cm^{-1} can be obtained with the 400 ps time gating, as shown in Fig. 9(i). With the 1.2 ns gating the Raman signal of olive oil can be said to be totally lost under the background, even though there is small hillock at 1434-1452 cm^{-1}, as shown in Fig. 9(e). The Raman signal of TiO_2 also starts to sink beneath the background with the 1.2 ns time gating, and with the 13 ns time gating, even the strong

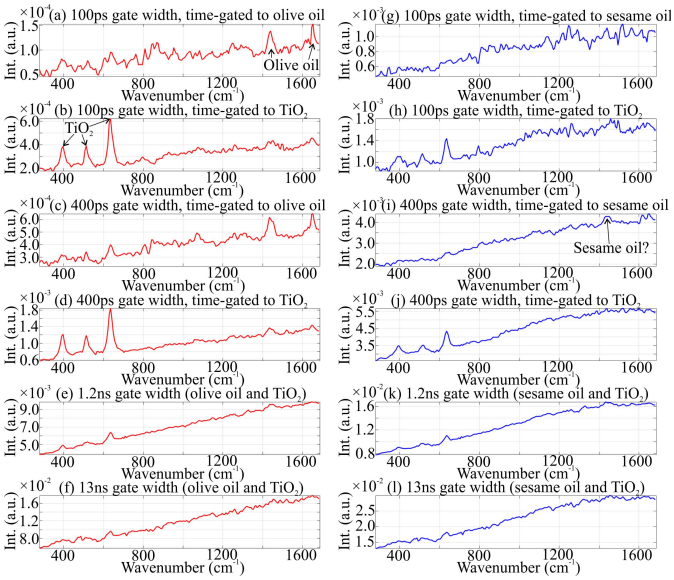

Fig. 9. Raman spectra measured from the medium in which (a)–(f) an olive oil target and TiO_2 target (red lines) or (g)–(l) a sesame seed oil and TiO_2 target (blue lines) was embedded using time-gate widths of 100 ps ((a) time-gated to olive oil, (g) to sesame oil, and (b), (h) to TiO_2), (e), (k) 1.2 ns and (f), (l) 13 ns.

peak at 635 cm^{-1} can only questionably be distinguished from the measured spectra, as shown in Figs. 9(e), 9(k), 9(f) and 9(l). Furthermore, the best SNR was achieved with the 400 ps time gating, as shown in Figs. 9(c), 9(d) and 9(j), but as mentioned above, this "long" time gate already has some unpleasant effects on depth derivation and Raman depth profiling performance. Thus, when selecting the time gate width in a certain situation it is important to consider what kind of information (depth or clear Raman spectra) will be of the most value at that time.

These results show the advantages of the adjustable picosecond time gating relative to the longer constant-sized time gates that are used in time-gated ICCDs, for example. It is also possible to construct short time gate structures by techniques other than CMOS technology, but the integration capability, compactness and "simplicity" of CMOS technology in this area is hard to beat. The weak spot that is usually related to SPAD sensors is the high dark count rate (DCR) of the detector, which may become a problem when samples with lower Raman signal levels are measured. The SPAD-based line sensor of the Raman spectrometer developed here was manufactured in a 0.35 μm high-voltage CMOS technology and the mean measured DCR of the sensor has been reported to be 128 Hz/μm^2 [37]. Nevertheless, median DCRs as low as 0.4 and 0.3 Hz/μm^2 have been reported with more modern 150 nm and 130 nm CMOS technologies, respectively [50], [51]. Therefore, one method for achieving a better SNR in future depth-resolving Raman spectrometers would be to use CMOS technologies and SPAD structures that have better noise performance in the sensor design. With better SNR either more difficult media with higher scattering properties could be measured, or smaller time gate widths could be used that would result in higher depth derivation and better Raman depth profiling performance.

IV. Conclusions

This paper presented a depth-resolving Raman spectrometer based on a pulsed laser, an adjustable time-gated 16×256 CMOS SPAD line sensor with a 256-channel TDC, a digital off-chip delay unit and a laptop-controlled adjustable coaxial delay unit. The technology concerned enables depth scanning with a verified variability of ± 0.43 cm in the derivation of depth information with samples embedded in a centimeter-scale semi-transparent medium simultaneously with normal Raman depth profiling. By virtue of the CMOS technology it is possible to integrate the delay and TCSPC electronics on the same die with the adjustable SPAD sensor and even time gate widths as short as 50 ps have already been achieved [37]. The technology developed here also allows modification of the width of the time gate not only before the measurements but also in the data post-processing phase. Thus, the size and complexity of the whole depth-resolving spectrometer would be markedly smaller if CMOS technology were used, and the adjustable picosecond time gating and delay scanning would be achieved more conveniently than with time-gated ICCDs, for example, in which longer constant-sized time gates are usually used. The short time gating obtained here was shown not only to increase the depth derivation and improve the Raman depth profiling performance but also to effectively suppress the fluorescence background even when samples having nanosecond-scale fluorescence lifetimes were measured. We believe that this kind of technology could pave the way for a new depth-resolving Raman spectrometer device for use in analytical applications involving the subsurface probing of semi-transparent media where a compact, practical device with a depth range of several centimeters is needed. Possible application areas for this technology could be e.g. quality monitoring in the food industry and nanocellulose manufacturing since Raman spectroscopy is already used in these areas and some of the analyzed media in these areas are transparent or semi-transparent [52], [53].

The SPAD sensor circuit was originally designed for being used with an earlier designed Raman microscope in which accurate time gate position scanning in small steps was not needed, and thus the digital off-chip delay unit and the adjustable coaxial delay unit were added to the system afterwards to achieve the necessary scanning functionality. Our main aim here was to show the depth-derivation capability and high performance of Raman depth profiling and fluorescence background suppression that is achievable with a CMOS technology-based SPAD line sensor as a proof of concept for depth-resolving Raman spectrometry. Future work will concentrate on development of the SPAD line sensor in order to narrow the IRF of the device, reduce the DCR of the detector and increase the level of integration of the line sensor with a high precision time gate position scanning functionality. A stabilized high resolution digital delay unit with a large delay range will be integrated into the same die with the SPAD sensor to achieve stable, accurate and wide scanning functionality. In addition, 3D Raman imaging of targets embedded in semi-transparent media and analysis of more turbid media with higher scattering properties than in the media used in this work will be on the agenda in the future to further investigate the possibilities of the concerned technology.

Acknowledgment

The authors want to thank Mr. Harri Juttula for helping us to estimate the absorption and reduced scattering coefficients of the media.

References

[1] N. A. Macleod and P. Matousek, "Deep noninvasive Raman spectroscopy of turbid media," *Appl. Spectrosc.*, vol. 62, no. 11, pp. 291A–304A, Nov. 2008.
[2] C. J. H. Brenan and I. W. Hunter, "Volumetric Raman microscopy through a turbid medium," J. Raman Spectrosc., vol. 27, no. 8, pp. 561–570, Aug. 1996.
[3] P. Matousek *et al.*, "Subsurface probing in diffusely scattering media using spatially offset Raman spectroscopy," *Appl. Spectrosc.*, vol. 59, no. 4, pp. 393–400, Apr. 2005.
[4] P. Matousek, "Inverse spatially offset Raman spectroscopy for deep noninvasive probing of turbid media," *Appl. Spectrosc.*, vol. 60, no. 11, pp. 1341–1347, Nov. 2006.
[5] N. Stone, K. Faulds, D. Graham, and P. Matousek, "Prospects of deep Raman spectroscopy for noninvasive detection of conjugated surface enhanced resonance Raman scattering nanoparticles buried within 25 mm of mammalian tissue," *Anal. Chem.*, vol. 82, no. 10, pp. 3969–3973, Apr. 2010.
[6] P. Matousek, C. Conti, M. Realini, and C. Colombo, "Micro-scale spatially offset Raman spectroscopy for non-invasive subsurface analysis of turbid materials," *Analyst*, vol. 141, no. 3, pp. 731–739, 2016.
[7] B. Gardner, P. Matousek, and N. Stone, "Temperature spatially offset Raman spectroscopy (T-SORS): Subsurface chemically specific measurement of temperature in turbid media using anti-Stokes spatially offset Raman spectroscopy," *Anal. Chem.*, vol. 88, no. 1, pp. 832–837, 2016.
[8] K. Buckley and P. Matousek, "Recent advances in the application of transmission Raman spectroscopy to pharmaceutical analysis," *J. Pharmaceutical Biomed. Anal.*, vol. 55, pp. 645–652, Jun. 2011.
[9] K. M. Khan, N. Ghosh, and S. K. Majumder, "Off-confocal Raman spectroscopy (OCRS) for subsurface measurements in layered turbid samples," *J. Opt.*, vol. 18, no. 9, Aug. 2016, Art. no. 095301.
[10] K. M. Khan, S. K. Majumder, and P. K. Gupta, "Cone–shell Raman spectroscopy (CSRS) for depth-sensitive measurements in layered tissue," *J. Biophoton.*, vol. 8, nos. 11–12, pp. 889–896, Nov. 2015.
[11] J. Wu, Y. Wang, L. Perelman, I. Itzkan, R. R. Dasari, and M. S. Feld, "Three-dimensional imaging of objects embedded in turbid media with fluorescence and Raman spectroscopy," *Appl. Opt.*, vol. 34, no. 18, pp. 3425–3430, Jun. 1995.
[12] P. Matousek, N. Everall, M. Towrie, and A. W. Parker, "Depth profiling in diffusely scattering media using Raman spectroscopy and picosecond kerr gating," *Appl. Spectrosc.*, vol. 59, no. 2, pp. 200–205, Feb. 2005.
[13] I. E. I. Petterson, P. Dvořák, J. B. Buijs, C. Gooijer, and F. Ariese, "Time-resolved spatially offset Raman spectroscopy for depth analysis of diffusely scattering layers," *Analyst*, vol. 135, no. 12, pp. 3255–3259, Oct. 2010.
[14] S. K. V. Sekar *et al.*, "Frequency offset Raman spectroscopy (FORS) for depth probing of diffusive media," *Opt. Express*, vol. 25, no. 5, pp. 4585–4597, Mar. 2017.
[15] P. Matousek and N. Stone, "Development of deep subsurface Raman spectroscopy for medical diagnosis and disease monitoring," *Chem. Soc. Rev.*, vol. 45, no. 7, pp. 1794–1802, 2016.
[16] C. Eliasson and P. Matousek, "Noninvasive authentication of pharmaceutical products through packaging using spatially offset Raman spectroscopy," *Anal. Chem.*, vol. 79, no. 4, pp. 1696–1701, Jan. 2007.
[17] C. Eliasson, N. A. Macleod, and P. Matousek, "Noninvasive detection of concealed liquid explosives using Raman spectroscopy," *Anal. Chem.*, vol. 79, no. 21, pp. 8185–8189, Sep. 2007.
[18] I. E. I. Petterson, M. López-López, C. García-Ruiz, C. Gooijer, J. B. Buijs, and F. Ariese, "Noninvasive detection of concealed explosives: Depth profiling through opaque plastics by time-resolved Raman spectroscopy," *Anal. Chem.*, vol. 83, no. 22, pp. 8517–8523, Oct. 2011.
[19] J. Qin, K. Chao, and M. S. Kim, "Nondestructive evaluation of internal maturity of tomatoes using spatially offset Raman spectroscopy," *Postharvest Biol. Technol.*, vol. 71, pp. 21–31, Sep. 2012.
[20] C. Conti, C. Colombo, M. Realini, and P. Matousek, "Subsurface analysis of painted sculptures and plasters using micrometre-scale spatially offset Raman spectroscopy (micro-SORS)," *J. Raman Spectrosc.*, vol. 46, no. 5, pp. 476–482, May 2015.

[21] J.-H. Hooijschuur, I. E. I. Petterson, G. R. Davies, C. Gooijer, and F. Ariese, "Time resolved Raman spectroscopy for depth analysis of multi-layered mineral samples," *J. Raman Spectrosc.*, vol. 44, no. 11, pp. 1540–1547, Nov. 2013.
[22] X. Dou, Y. Yamaguchi, H. Yamamoto, H. Uenoyama, and Y. Ozaki, "Biological applications of anti-Stokes Raman spectroscopy: Quantitative analysis of glucose in plasma and serum by a highly sensitive multichannel Raman spectrometer," *Appl. Spectrosc.*, vol. 50, no. 10, pp. 1301–1306, Oct. 1996.
[23] J. Blacksberg, Y. Maruyama, E. Charbon, and G. R. Rossman, "Fast single-photon avalanche diode arrays for laser Raman spectroscopy," *Opt. Lett.*, vol. 36, no. 18, pp. 3672–3674, Sep. 2011.
[24] Y. Fleger, L. Nagli, M. Gaft, and M. Rosenbluh, "Narrow gated Raman and luminescence of explosivesc," *J. Lumin.*, vol. 129, no. 9, pp. 979–983, Sep. 2009.
[25] D. V. Martyshkin, R. C. Ahuja, A. Kudriavtsev, and S. B. Mirov, "Effective suppression of fluorescence light in Raman measurements using ultrafast time gated charge coupled device camera," *Rev. Sci. Instrum.*, vol. 75, no. 3, pp. 630–635, Mar. 2004.
[26] P. Matousek *et al.*, "Fluorescence suppression in resonance Raman spectroscopy using a high-performance picosecond Kerr gate," *J. Raman Spectrosc.*, vol. 32, no. 12, pp. 983–988, Dec. 2001.
[27] F. Ariese, H. Meuzelaar, M. M. Kerssens, J. B. Buijs, and C. Gooijer, "Picosecond Raman spectroscopy with a fast intensified CCD camera for depth analysis of diffusely scattering media," *Analyst*, vol. 134, no. 6, pp. 1192–1197, Mar. 2009.
[28] S. K. V. Sekar *et al.*, "Time domain diffuse Raman spectrometer based on a TCSPC camera for the depth analysis of diffusive media," *Opt. Lett.*, vol. 43, no. 9, pp. 2134–2137, 2018.
[29] F. Martelli, T. Binzoni, A. Pifferi, L. Spinelli, A. Farina, and A. Torricelli, "There's plenty of light at the bottom: statistics of photon penetration depth in random media," *Sci. Rep.*, vol. 6, Jun. 2016, Art. no. 27057.
[30] F. Martelli, T. Binzoni, S. K. V. Sekar, A. Farina, S. Cavalieri, and A. Pifferi, "Time-domain Raman analytical forward solvers," *Opt. Express*, vol. 24, no. 18, pp. 20382–20399, Sep. 2016.
[31] I. E. I. Petterson, F. W. L. Esmonde-White, W. de Wilde, M. D. Morris, and F. Ariese, "Tissue phantoms to compare spatial and temporal offset modes of deep Raman spectroscopy," *Analyst*, vol. 140, no. 7, pp. 2504–2512, Feb. 2015.
[32] C. Zhang, L. Zhang, R. Yang, K. Liang, and D. Han, "Time-correlated Raman and fluorescence spectroscopy based on a silicon photomultiplier and time-correlated single photon counting technique," *Appl. Spectrosc.*, vol. 67, no. 2, pp. 136–140, Feb. 2013.
[33] Y. Prokazov, E. Turbin, A. Weber, R. Hartig, and W. Zuschratter, "Position sensitive detector for fluorescence lifetime imaging," *J. Instrum.*, vol. 9, no. 12, Dec. 2014, Art. no. C12015.
[34] I. Nissinen *et al.*, "A sub-ns time-gated CMOS single photon avalanche diode detector for Raman spectroscopy," in *Proc. ESSDERC*, Helsinki, Finland, Sep. 2011, pp. 375–378.
[35] J. Kostamovaara, J. Tenhunen, M. Kögler, I. Nissinen, J. Nissinen, and P. Keränen, "Fluorescence suppression in Raman spectroscopy using a time-gated CMOS SPAD," *Opt. Express*, vol. 21, no. 25, pp. 31632–31645, Dec. 2013.
[36] I. Nissinen, A.-K. Länsman, J. Nissinen, J. Holma, and J. Kostamovaara, "2×(4×)128 time-gated CMOS single photon avalanche diode line detector with 100 ps resolution for Raman spectroscopy," in *Proc. ESSCIRC*, Bucharest, Romania, Sep. 2013, pp. 291–294.
[37] I. Nissinen, J. Nissinen, P. Keränen, D. Stoppa, and J. Kostamovaara, "A 16×256 SPAD Line Detector With a 50-ps, 3-bit, 256-channel time-to-digital converter for Raman spectroscopy," *IEEE Sensors J.*, vol. 18, no. 9, pp. 3789–3798, May 2018.
[38] Y. Maruyama, J. Blacksberg, and E. Charbon, "A 1024×8, 700-ps time-gated SPAD line sensor for planetary surface exploration with laser Raman spectroscopy and LIBS," *IEEE J. Solid-State Circuits*, vol. 49, no. 1, pp. 179–189, Jan. 2014.
[39] Z. Li, M. J. Deen, S. Kumar, and P. R. Selvaganapathy, "Raman spectroscopy for in-line water quality monitoring-instrumentation and potential," *Sensors*, vol. 14, no. 9, pp. 17275–17303, Sep. 2014.
[40] A. T. Erdogan, R. Walker, N. Finlayson, N. Krstajic, G. O. S. Williams, and R. K. Henderson, "A 16.5 giga events/s 1024×8 SPAD line sensor with per-pixel zoomable 50 ps-6.4 ns/bin histogramming TDC," in *Proc. Symp. VLSI Circuits*, Kyoto, Japan, Aug. 2017, pp. C292–C293.
[41] J. Kekkonen, J. Nissinen, J. Kostamovaara, and I. Nissinen, "Distance-resolving Raman radar based on a time-correlated CMOS single-photon avalanche diode line sensor," *Sensors*, vol. 18, no. 10, p. 3200, Sep. 2018.
[42] J. Holma, I. Nissinen, J. Nissinen, and J. Kostamovaara, "Characterization of the timing homogeneity in a CMOS SPAD array designed for time-gated Raman spectroscopy," *IEEE Trans. Instrum. Meas.*, vol. 66, no. 7, pp. 1837–1844, Jul. 2017.
[43] H. G. Akarçay, S. Preisser, M. Frenz, and J. Rička, "Determining the optical properties of a gelatin-TiO_2 phantom at 780 nm," *Biomed. Opt. Express*, vol. 3, no. 3, pp. 418–434, Mar. 2012.
[44] T. A. Dolenko *et al.*, "Raman spectroscopy of water–ethanol solutions: The estimation of hydrogen bonding energy and the appearance of clathrate-like structures in solutions," *J. Phys. Chem. A*, vol. 119, no. 44, pp. 10806–10815, Oct. 2015.
[45] T. Ohsaka, F. Izumi, and Y. Fujiki, "Raman spectrum of anatase, TiO_2," *J. Raman Spectrosc.*, vol. 7, no. 6, pp. 321–324, Dec. 1978.
[46] McCreery Research Group. (2014). *Standard Spectra*. Accessed: Oct. 12, 2018. [Online]. Available: http://www.chem.ualberta.ca/~mccreery/ramanmaterials.html#toluene
[47] I. Z. Kozma, P. Krok, and E. Riedle, "Direct measurement of the group-velocity mismatch and derivation of the refractive-index dispersion for a variety of solvents in the ultraviolet," *J. Opt. Soc. Amer. B, Opt. Phys.*, vol. 22, no. 7, pp. 1479–1485, Jul. 2005.
[48] J. R. DeVore, "Refractive indices of rutile and sphalerite," *J. Opt. Soc. Amer. B, Opt. Phys.*, vol. 41, no. 6, pp. 416–419, 1951.
[49] I. Nissinen, J. Nissinen, P. Keränen, and J. Kostamovaara, "On the effects of the time gate position and width on the signal-to-noise ratio for detection of Raman spectrum in a time-gated CMOS single-photon avalanche diode based sensor," *Sens. Actuators B, Chem.*, vol. 241, pp. 1145–1152, Mar. 2017.
[50] H. Xu, L. Pancheri, G.-F. D. Betta, and D. Stoppa, "Design and characterization of a p+/n-well SPAD array in 150 nm CMOS process," *Opt. Express*, vol. 25, no. 11, pp. 12765–12778, May 2017.
[51] E. A. G. Webster, L. A. Grant, and R. K. Henderson, "A high-performance single-photon avalanche diode in 130-nm CMOS imaging technology," *IEEE Electron Device Lett.*, vol. 33, no. 11, pp. 1589–1591, Nov. 2012.
[52] D. Yang and Y. Ying, "Applications of Raman spectroscopy in agricultural products and food analysis: A review," *Appl. Spectrosc. Rev.*, vol. 46, no. 7, pp. 539–560, Oct. 2011.
[53] U. P. Agarwal, R. Sabo, R. S. Reiner, C. M. Clemons, and A. W. Rudie, "Spatially resolved characterization of cellulose nanocrystal–polypropylene composite by confocal Raman microscopy," *Appl. Spectrosc.*, vol. 66, no. 7, pp. 750–756, Jul. 2012.

Jere Kekkonen received the M.S. degree in medical and wellness technology from the University of Oulu, Finland, in 2018, where he is currently pursuing the Ph.D. degree in electrical engineering with the Circuits and Systems Research Unit.

His research interests include novel functionalities and applications of time-resolved Raman spectroscopy systems based on CMOS SPAD sensors.

Jan Nissinen received the M.Sc. (Eng.) and Dr.Tech. degrees in electrical engineering from the University of Oulu, Finland, in 2002 and 2011, respectively.

He has been a Post-Doctoral Researcher with the Circuits and Systems Research Unit, University of Oulu, since 2011. His research interests include the design of analog and mixed-signal integrated circuits for pulsed time-of-flight laser rangefinders and for pulsed Raman spectroscopy.

Ilkka Nissinen (M'09) received the M.Sc. (Eng.) and Dr.Tech. degrees in electrical engineering from the University of Oulu, Finland, in 2002 and 2011, respectively.

From 2018 to 2023, he was an Associate Professor of Analogue and Mixed-Signal Microelectronic Circuit Design with the Circuits and Systems Research Unit, University of Oulu. His research interests include the design of time interval measurement architectures for the integrated sensors of pulsed time-of-flight laser technologies.